Acknowledgements

I would like to express my gratitude towards the people who have helped and provided support to me throughout the course of this project without whom the research would not have been possible.

Most notably I would like to thank Professor Gopal Madabhushi for his guidance; the PhD students in Geotechnical Engineering at CUED including Abdul Zeybek, Srikanth Madabhushi and Stefan Ritter who were able to offer valuable experience-based advice throughout; and the technicians at the Schofield Centre for Geotechnical Process & Construction Modelling where the tests were conducted.

Contents

1 Introduction

This report presents the background, process and findings of an experimental research project into the floatation of underground structures during earthquake induced liquefaction specifically that of rectangular sectioned tunnels. The report includes information about the motivation for conducting the research, reviews literature of previous investigations and details the process and outcomes of these experiments.

1.1 Motivation

1.1.1 Urban populations, resources and construction

Throughout human history the globe's population has grown at an increasing rate with rare exception. The distribution of this growing population has been far from uniform; rather it is concentrated in pockets of varying size and density. This non-uniform growth has led to the formation of urban centres. Here the highest population densities are often found bringing the residential, commercial, industrial and other urban land uses that come with it. In 1960 only 34% of the world's population lived in urban areas, today the figure is 54% and rising [1]. As a result of this growth the demands placed on infrastructure and the competition for space are significantly greater than they were fifty years ago. Another effect is that people have become more efficient in the way they use land. Techniques of construction above and below ground have seen large development enabling larger population densities and concentration of services and commercial land use.

Many of today's built environments are situated in seismically active regions such as on the Pacific Rim in Far-East Asia and Western America. Cities such as Tokyo, Santiago and Los Angeles are all at high risk from tectonic movements [2]. These risks are often in the form of earthquakes which can have a damaging effect on above-ground structures but also on underground structures such as pipelines and tunnels that are used for resource distribution, waste disposal and transport of goods and people.

1.1.2 Earthquake damage

Earthquakes can affect structures directly through damage caused by the shaking motion and through permanent ground displacement at plate boundaries but also indirectly through phenomena such as soil settlement and liquefaction. Liquefaction is a temporary change in a soil's macroscopic mechanical properties such that it is able to flow as a viscous fluid. It occurs under certain conditions in loosely packed sandy soils that have a tendency to contract when disturbed. Section 2.1 describes the phenomenon in more detail.

In this investigation 'heavy' structures are classed as structures that are more dense than the surrounding pore fluid (e.g. water, found in gaps between particles of saturated soil). Heavy structures often sink in liquefied soil, as seen in the sinking and rotation of a Japanese apartment block, Figure 1 [3]. 'Light' structures (less dense than their surrounding pore fluid) are often seen to experience buoyant uplift in floatation during liquefaction as seen in Figure 2 [4] and Figure 3 [5].

The direct and indirect effects of earthquakes can cause severe damage to underground structures thereby cutting off transport links and inhibiting the distribution of resources such as water and electrical power. This can be particularly harmful during the early stages of disaster relief when such resources are vital for the wellbeing of survivors and the efforts of emergency services. In the longer term, effects on public health can become a concern as a result of the damages for example when waste systems are disrupted and water-borne diseases can prevail due to build-up of stagnant sewage that contaminates drinking water as experienced in the Christchurch, New Zealand earthquakes of 2011 [6].

Figure 1 - Sinking of 'heavy' structure - Niigata, Japan 1964

Figure 2 - Floatation of piping and inspection cover - Chuetsu, Japan 2004

Figure 3 - Floatation of underground storage tanks - Tokyo, Japan 2011

1.2 Project Aims

With the motivation of contributing to the wider research of earthquake engineering which is vital to the preservation of life and well-being this investigation aims to add to the understanding of how rectangular tunnels respond to earthquake loading in liquefiable soils. This will be achieved by conducting a series of dynamic experimental tests to measure the displacement and inertial response of a model tunnel embedded in a mass of saturated sand subjected to earthquake. In addition the mechanism by which the surrounding soil fails in the event of tunnel floatation will be visualised using image processing techniques.

2 Literature Review

2.1 Liquefaction

Liquefaction is a phenomenon whose effects are observed frequently as a result of earthquakes all around the world. There are specific conditions that enable soil to undergo liquefaction in relation to the soil constituents and imposed inertial conditions. These specific conditions enable the mechanism of liquefaction to occur and have implications for the design of the experimental tests.

2.1.1 Soil conditions

In order for the ground to be susceptible to liquefaction it needs to consist of soil at low relative density, $I_R \approx 40\%$, such that the loosely packed structure of the soil particles causes a tendency for it to contract into a more densely packed arrangement when disturbed. The soil must be saturated with fluid to ensure incompressibility in the pore spaces and it must also have a low to medium permeability (around 10^{-4} m/s) that impedes the flow of pore fluid through the inter-granular voids imposing undrained conditions for the duration of disturbance. Pore spaces are usually saturated with water containing some aqueous phase solutes.

2.1.2 Inertial conditions

The mode of disturbance that causes the most marked contractile tendency in loosely packed particulate materials like soil is shearing. In this case parallel layers of particles are forced to slip past one another and the surfaces position themselves in the configuration of lowest potential. Undrained conditions occur when loading is much faster than the dissipation of excess pore pressures. Earthquake loading frequently fulfils this criterion.

2.1.3 Liquefaction mechanism

During earthquake loading shear waves are propagated through the soil at high speed causing the soil to try to contract. Contraction is resisted by the soil's pore fluid that is unable to give way to the soil granules as it cannot reduce in volume and cannot escape from the pore spaces quickly enough. As a result undrained conditions occur and positive excess pore pressures, Δu, are produced [7].

Throughout the loading the total vertical stress, σ_v, remains unchanged as the same bulk mass of soil and water above any reference depth remains the same. Similarly the total horizontal stresses, σ_h, remain the constant. As a result of this and the increase of pore water pressures the effective stresses decrease according to Terzaghi's Principle in the following equation.

$$\sigma' = \sigma - u \tag{1}$$

where $u = u_o + \Delta u$, the sum of hydrostatic and excess pore pressures.

As the effective stress decreases, the normal contact force between particles decreases which lowers the bearing friction capacity allowing particles to slip by one another with greater ease. The soil's shear strength is reduced significantly until the pore pressure becomes equal to total stress and the soil behaves like a fluid with very little shear capacity.

2.1.4 Experimental implications

The types of soil that are most likely to achieve the required characteristics of low relative density and low to medium hydraulic conductivity in tandem are sand-sized and smaller. It is also noted that the particles must not have significant cohesive properties like in clay. This leaves the most appropriate soil types as sands and silts within the approximate particle size range of 0.07mm to 5mm.

In order to simulate the fast shear loading of earthquakes it will be necessary to use apparatus that has the ability to shake a sample of adequate size in the horizontal plane. To this end the 1-g shaking table at the Schofield Centre, West Cambridge will be used.

2.2 Previous Work

A number of investigations into the floatation of tunnels in earthquake induced liquefaction have been carried out prior to this. Between them they have considered various aspects of the response and relate to the experiments differently.

For the purposes of this investigation the depth below soil surface level to which a tunnel is buried is expressed as a non-dimensional number known as the 'Burial Ratio', R_b. Burial Ratio is defined as the ratio between the vertical distance between the soil surface and the centroid of the tunnel or, expressed in the following algebraic form where d and w are shown on Figure 10:

$$Burial\ Ratio, R_b = \frac{d}{w} \tag{2}$$

2.2.1 E Room (2014)

Similar experiments to those that are to be carried out as part of this investigation were carried out by Room (2015) [8]. Room's investigation provides information through experience on experimental methods similar to those that are to be used during this investigation. Much of the same experimental apparatus will be employed, a full description of the experimental set-up is included later but omitted here for brevity.

In the experiment a base sinusoidal input of 5Hz at 5mm amplitude was used for each test for a total input duration of 10s. Throughout the experiments the base input acceleration, the tunnel's horizontal acceleration and vertical displacement and the pore pressure beneath the invert of the tunnel were measured.

A 44 frame per second GoPro camera was used in these tests to film the response through a translucent side of the test box. 44FPS was adequate for Room's investigation due to the fact that the footage was only used to record visual observations. In this investigation a greater frequency of image capture will be required in order to provide adequate results for PIV analysis. The target imaging frequency is 20 frames per earthquake cycle correlating to 100Hz imaging frequency. This rate of image capture will be achieved by using a 'MotionBlitz' high speed camera.

The measurements of pore pressure beneath the tunnel invert correlate well with the prediction of Madabhushi's finite element model described in section 2.2.2. The measurements confirm that a rise in excess pore pressure occurs when shaking begins however a field of negative excess pore pressures is superposed on this beneath the tunnel's invert when floatation uplift occurs. The excess pore pressures dissipate exponentially halving in five seconds suggesting that they will dissipate to less than 5% of their peak after less than 30s after the last earthquake cycle. This is to be used as a guideline for any successive earthquakes applied in this test.

Tunnel burial depth was varied between experiments for burial ratios, R_b = 0.45, 0.7 and 1.2. In the shallowest test (R_b = 0.45) the tunnel was able to rise out of the sand's surface limiting the extent of total uplift due to the neutrally buoyant position where the tunnel would no longer tend to float because of the reduction in buoyant forces as more of the tunnel is exposed, out of the liquefied soil.

In the experiment Room was also able to provide an estimate of the soil's displacement mechanism during the floatation by visual observation as represented in Figure 4. It was observed that the sand is pushed away to the either side of the tunnel from in front of the tunnel's motion (above the tunnel crown) and that it flows round the tunnel sides. Sand is also drawn in from the side and beneath the tunnel as it is sucked towards the tunnel invert in the low pressure area resulting from tunnel uplift movement. The tunnel was also seen to finish in all experiments at a rotated angle, the greatest rotation occurring for the test at shallowest burial depth. A similar deformation mechanism form will be expected in the shaking tests of this experiment however they will be represented using PIV tracking to provide a more accurate flow pattern with better estimates of the distance of movement of each patch of soil and the extent to which the soil further away from the tunnel is affected.

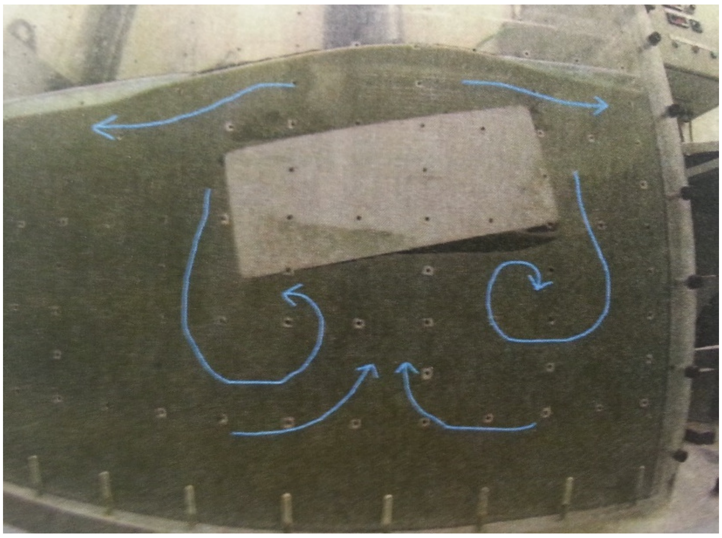

Figure 4 - Representation of soil failure mechanism for R_b = 0.7, Room (2014) [8]

2.2.2 SSC Madabhushi (2014)

In the paper entitled 'Finite Element Analysis of Floatation of Rectangular Tunnels Following Earthquake Induced Liquefaction' Madabhushi constructs a finite element model of a rectangular tunnel in saturated sand. The sand was modelled to have similar properties to those used at the Schofield Centre and the tunnel was modelled with the same cross-sectional aspect ratio as that of the physical model used in these experiments with its width (10m) being 2.5 times the height (4m). The dimensions are suitable for a cut and cover tunnel housing a two-way railway. The finite element model placed the tunnel with its centroid at 12m below the soil surface. This burial depth corresponds to $R_b = 1.2$.

Madabhushi's model was used to predict the tunnel uplift, excess pore pressure generation and soil surface heave in response to a ramped sinusoidal input and a more realistic base acceleration input imitating that of the 1995 Kobe Earthquake in Japan with peak base accelerations of 0.5g and 0.8g respectively. Accelerations of a similar order of magnitude can be reached during 1-g shaking table tests at the Schofield Centre.

The model used the assumption of plane strain due to the considerable length of the tunnel in comparison to its cross-sectional dimensions. The boundary conditions for the edges of the soil domain were fixed in the horizontally but free to move vertically. In the physical experimental tests this complete freedom of the soil to move in the vertical direction at the boundaries may be difficult to achieve due to friction between the container and the sand. Though the x-direction would likely be fixed also in a physical model this is not necessarily the most accurate representation of a real-life situation where the soil is very rarely rigidly contained at the lateral extents. Despite this, the similarity between the finite element and physical model in this respect will enable results to be comparable.

The finite element model investigation considered the isolation of the tunnel and the soil surface accelerations from the base node accelerations due to the effect of liquefaction. These results can be used as an indicator of the delay of onset of liquefaction in a physical model comparing it to the timing of responses such as uplift and soil heave.

The FE model also provided information about the generation of excess pore pressures during the earthquake. It was found that positive excess pore pressures were generated beneath the invert of the tunnel during liquefaction in agreement with the theory presented in section 2.1.3. The FE model also provides insight into how the pore pressures change as the tunnel undergoes floatation. These results showed that the upward motion a field of negative excess pore pressures is superimposed with the positive excess pore pressure creating a suction force that slows down the rate of uplift.

2.2.3 S Chian

Centrifuge earthquake tests have been carried out on circular tunnels prior to this investigation by Chian et al (2010, 2012) at the Schofield Centre, West Cambridge. The experiments found that increasing the burial depth of a tunnel reduced the amount by which it was able to uplift as a result of floatation in soil liquefaction [9]. The research, presented in various papers used PIV analysis to plot the cumulative and quarter-cycle soil displacements, an example of which is show in Figure 5 and used as a comparison in later chapters.

With close similarity to the soil deformations observed by Room, Chian's circular tunnel tests see an upward movement of the tunnel in floatation forcing the sand directly above it upwards and to either side as shown by the large arrows representing the general motion. Soil moves down the sides of the tunnel coming round to fill in the space beneath the invert of the tunnel. The suction of the soil up behind the tunnel is driven by the excess negative pore pressures predicted by Madabhushi's finite element model [7] and confirmed by Room's pore pressure measurement [8].

Chian also found that tunnel floatation has a two dimensional track in the plane of a diametric cross-section. The tunnel's movement deviates away from a line drawn vertically from starting to finishing position.

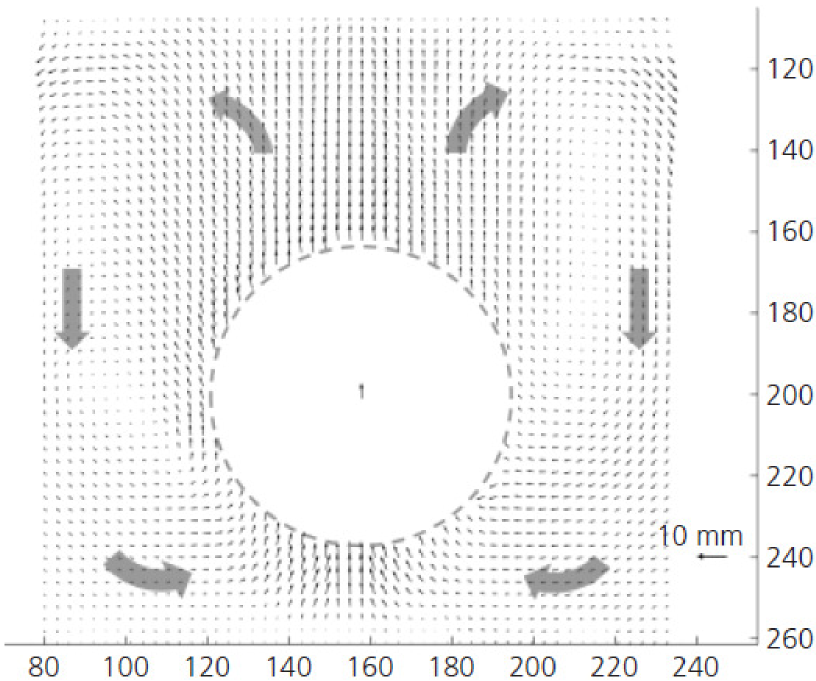

Figure 5 – Cumulative displacement vectors of soil and structure in a centrifuge test obtained from particle image velocimetry analysis (Chian and Madabhushi, 2010) [10]

2.3 Visualisation Technique – PIV Analysis

The visualisation technique selected for the visualisation of the soil failure mechanisms in this investigation is Particle Image Velocimetry referred to as 'PIV'. It is a technique that was initially developed for application to visualising three dimensional flows in the field of fluid mechanics but has been adopted by civil engineers for various applications such as the monitoring of crack formation on the surface of concrete members and the settlement of structural foundations. A visualisation technique for planar soil deformation was developed by White, Take and Bolton (2003) that uses digital photogrammetry and PIV. It was shown to produce results that were an order of magnitude more precise than any similar techniques of the time [11]. In this particular experiment PIV is expected to give an accurate representation of soil deformation as it flows around the floating tunnel structure.

2.3.1 Image processing overview

An application of this method analyses digital images using a software developed as described in the technical report of the authors [12]. The PIV software works by tracking the movement of patches of an image of a textured surface. It does this by dividing each image into a grid of test patches of a defined width, height and spacing as shown in Figure 6. For each test patch in image 1 (the reference image) it produces a larger search patch centred on the same u-v coordinates on image 2 (the deformed image). By iterating the position of a test patch inside the search patch on image 2 and calculating the degree of match (or correlation) of the pixel intensities of the textured surface for each iteration the new position of the reference patch in the deformed image is determined as where the coordinates have the greatest degree of match.

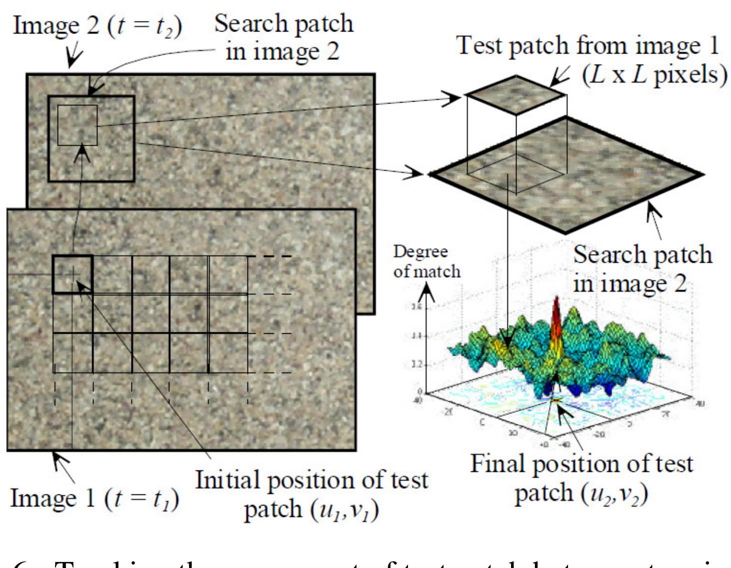

Figure 6 - Tracking the movement of test patch between two images [12]

This process is repeated for each test patch in the reference image to achieve a field of vectors that represent the movement of test patches from the reference to deformed image. This is often displayed in a quiver plot where vector arrows point in the direction of movement of each patch with the arrow length corresponding to liner deformation magnitude.

2.3.2 Further processing

The initial PIV processing creates deformation vectors in the u-v coordinate system of the digital images. Though these images can often provide a good qualitative description of deformations they are susceptible to inaccuracy as a result of distortions such as lens aberration. They lack a physical scale and any relative motion between the imaging camera and the apparatus will be included as a component of displacement vectors. In order to mitigate these issues the deformation plots are calibrated by reference to control markers that are fixed at the interface between the specimen and viewing boundary. The positions of the control markers that are fixed relative to the shaking table are tracked and their displacement is subtracted from that of the soil and tunnel giving displacements relative to the shaking table. A grid of dots of known spacing printed on what is known as a 'Mylar card' is photographed digitally in place of the model before testing the specimen to provide a length scale to calibrate the deformation vector lengths. This process brings the soil deformations from image space (U, V coordinates system) to model space (X, Y coordinates).

2.3.3 Limitations

When applied in geotechnics PIV is usually used in the imaging of opaque materials only the outer surface of a specimen can be viewed. As a result of this any test apparatus must be set up such that the imaged surface is representative of the whole sample and not significantly affected by any boundaries imposed by the test setup.

PIV also uses a significant amount of digital memory in storing the images once they have been taken and it can be demanding on computing power when processing the images as described in section 2.3.1.

3 Experimental Setup

This section outlines the setup of experimental apparatus and how it was used to gather the required data for necessary analysis. The apparatus assembly has a resemblance to that of previous tests carried out in the same laboratory following the work of Room (2014) and, less closely, the work of Chian (2013).

3.1 Apparatus

There were various components to the test apparatus as described in the following sections. Figure 7 below provides an overall view of the experimental setup as a photograph from behind the apparatus.

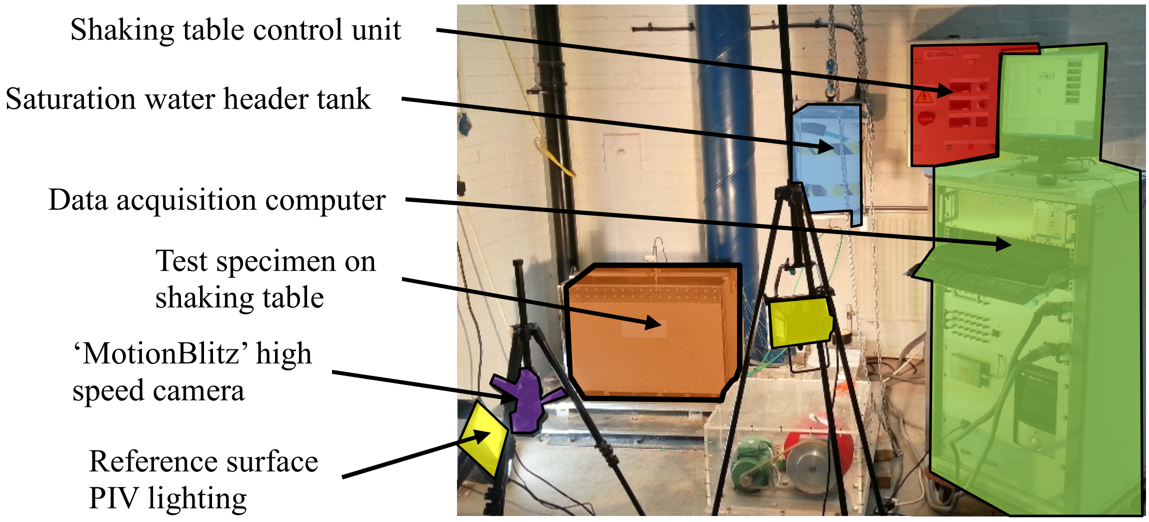

Figure 7 – layout of experimental setup

3.1.1 Test subject

The test subject has two main components, the saturated sand that is to be liquefied and the model tunnel that is buried at a variable depth within the sand.

In section 2.1.1 the soil conditions required for liquefaction to occur were set out and as a result the sand known as 'Hostun sand' was selected for use. The Hostun sand was poured at a relative density of I_D = 40% with corresponding voids ratio, e = 0.828, as shown in Figure 8 with the other soil parameters. In order to enhance the optical texture of the soil to aid PIV analysis one tenth of the mass of sand was dyed blue and mixed evenly throughout the sand. The image of Figure 9 shows the sand at the beginning and end of the mixing process.

Parameter	Value
Gs	2.65
e_{max}	1.01 [13]
e_{min}	0.555 [13]
I_D (%)	40
e	0.828
γ_{bulk} (kNm^{-3})	18.64

Figure 8 – Hostun sand parameters for testing

Figure 9 - 10:1 ratio PIV sand mix before and after mixing

After mixing, the sand was then manually poured into the test container in the most uniform fashion possible according to the necessary fall height and nozzle aperture width to achieve the appropriate relative density as previously calibrated. It was found that the most consistent way to achieve uniform density was by pouring layer by layer alternating the nozzle motion between parallel lines lengthways and widthways inside the test container. At the appropriate depth of sand had been poured the model tunnel was positioned according to the required burial ratio (depth to tunnel centroid divided by tunnel width) before pouring was resumed and completed.

The next stage of setup was to saturate the sand. It was determined that introducing water from the top sand surface would risk trapping air bubbles in the sand voids. Instead the sand was saturated from the bottom up so that air initially filling the voids would be pushed out upwards towards the open surface. Appendix B includes photographs of the apparatus used for pouring and saturation of the sand.

The model tunnel section had a mass of 2.5kg and dimensions of width 200mm, height 80mm and length 300mm. The body of the model was fabricated from folded aluminium sheeting capped at each end with white Teflon sheets that were secured by a bonding agent. The tunnel was hollow and water tight so that the centre would not allow the ingress of water throughout the duration of experiment setup and testing. The model tunnel was assumed fully rigid for the purposes of the experiment.

In real conditions where a tunnel may be many kilometres long plane strain conditions may be assumed due to the length being much greater than height or width. By placing this model tunnel section tightly between two sides of the test container it was assumed to be consistent with the plane strain condition.

3.1.2 Shaking table

The test specimen inside its box was placed on a shaking table which was capable of producing sinusoidal displacement outputs of variable duration, frequency and amplitude up to 60s, 4Hz and 5mm respectively at 1-g. These parameters were to be set and fixed before each shaking test. In reality earthquakes have a spectrum of frequencies in their ground movement however a single frequency sinusoidal shaking is able to produce sufficient acceleration to cause liquefaction.

3.1.3 Instrumentation and data acquisition

With the test specimen in place a system of sensors was designed to record the response of the tunnel during testing. Various instruments were included in the design including Microelectromechanical System (MEMS) Accelerometers, Piezoelectric Accelerometers, Linear Voltage Displacement Transducers (LVDT), Draw-wire Potentiometers (DWP) and Pore Pressure Transducers (PPT). While capturing the necessary information about the model's response the instrumentation network was designed to reduce the amount of influence it might have on the response. To achieve this instruments were selected to be small in relation to the test apparatus dimensions and positioned such that the influence on the results would be minimal. For instance the draw-wire potentiometer was attached such that any tension in the wire would cause no net moment on the tunnel.

The instrumentation produced continuous analogue voltage outputs which were detected and sampled by a data acquisition computer when connected via a junction box.

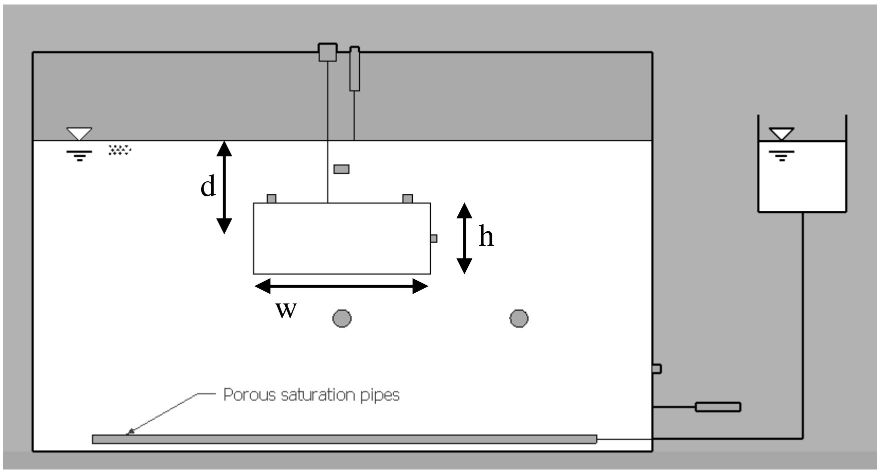

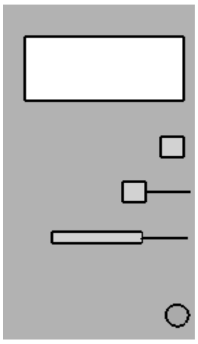

Key
-Tunnel cross-section
-Accelerometer
-Draw-wire potentiometer
-Linear Voltage Displacement Transducer
-Pore Pressure Transducer

Figure 10 - Instrumentation Schematic (approximate scale 1:10)

3.1.4 PIV apparatus

PIV analysis requires specific controlled conditions and apparatus to enable it to be carried out. The primary piece of equipment required for capturing images of the dynamic response was a high speed camera. In this experiment a 'MotionBlitz' camera capable of capturing images at thousands of frames per second was used. Due to the high frame rate, shutter time was limited which affected the amount of light able to enter through the camera aperture in each photograph. As a result intense lighting was required for illuminating the surface of the specimen through a transparent plastic sheet that formed the front side of the test container through which photographs of the sand and tunnel would be taken.

The transparent plastic container side was marked with a grid of black dots called control markers which would be used in the PIV deformation calibration as described in section 2.3.2. It was important to ensure that the control markers were spaced at a great enough density such that the area of interest in any analysis would contain 14 control markers, an adequate number for reliable calibration later on. Despite this requirement for high density of control markers it was also noted that the control markers should not be spaced too close together such that a large proportion of the soil reference section would be obscured from view limiting the information available for PIV analysis.

3.2 Overview of Experiments

In order to achieve the desired research objectives the apparatus previously described was used in a sequence of shaking table tests. Four tests were carried out in total and the single variable that was changed between each test was the depth at which the tunnel was buried in the Hostun sand. For the four tests in sequence burial ratio, $R_b = 0.5; 1.0; 0.25; 0.75$.

In each test the shaking table was initially set to shake at a frequency of 4Hz with an amplitude of 3mm producing a peak base acceleration of = $(2\pi.4)^2(.003) = 1.89ms^{-2} = 0.19g$. Research has shown that this is above the threshold peak ground acceleration required to cause liquefaction, 0.08g [14]. In the tests carried out by Room (2014) a slightly greater acceleration was more than sufficient to cause liquefaction of the sand in a similar setup with similar apparatus.

3.3 Adaptations to Experimental Set-up

Some adaptations were made to the test apparatus after Test 1 including the removal of PPTs from future tests due to the lack of sensitivity of the instruments available at the laboratory making the previously used instruments redundant. The removal of PPTs was deemed to have negligible effect on the test results due to their size and mass being far smaller than the tunnel and container. Additionally the draw-wire potentiometer was included in the test set-up from Test 2 onwards due to delays in fabrication of a suitable rig to hold the DWP in place which meant it not possible to include it for Test 1.

3.4 Prediction of Floatation

Before the experiments were carried out calculations were made to guide predictions as to whether or not the model tunnel would undergo floatation during liquefaction. The calculations were based on a simple model outlined in Appendix A: Buoyancy calculations. The model considers the forces acting on the tunnel due to its self-weight, buoyancy in the liquefied soil and overburden pressure from the directly overlying soil. The model negates any possible friction capacity between the overlying block of sand and the adjacent sand – assuming complete liquefaction.

The calculations produce a ratio between the upward and downward forces called the 'floatation factor (FF)'. Floatation is expected to occur for FF>1. A greater Floatation Factor corresponds to an increased likelihood of floatation.

Test	R_b	**d (m)**	F_{up} **(kN)**	F_{down} **(kN)**	**FF=** F_{up}/F_{down}
1	0.5	0.100	0.188	0.0563	3.34
2	1.0	0.200	0.188	0.1093	1.72
3	0.25	0.050	0.188	0.0298	6.31
4	0.75	0.150	0.188	0.0828	2.27

Figure 11 - Floatation Factor calculations

The calculations suggest that each of the tests will lead to floatation of the model tunnel. In test two, where the tunnel is buried the deepest the floatation factor is the smallest, the floatation factor is at a minimum and therefore floatation is least likely.

With increasing depth the confining pressures on the sand are increased and as a result the effective stresses to be overcome by excess pore pressures are greater. Full liquefaction is therefore less likely to occur in the tests of greater R_b. Liquefaction will be confirmed by analysis of acceleration data to determine the degree of inertial isolation between the tunnel and shaking table base.

4 Data Acquisition and Processing

Once the apparatus had been set up and monitoring equipment made ready the tests could be carried out. During each test output signals were produced by each of the monitoring instruments and photographs were taken by the high speed camera. Some specific conditions were required in order to be able to gather this data and once it had been recorded it could be processed to provide meaningful information for further interpretation and analysis.

4.1 Instrumentation

4.1.1 Raw data signals

The measuring instruments described in section 3.1.3 were connected to a computer that sampled the voltage outputs of the instruments at a frequency of 1000Hz. This meant that aliasing due to sparse sampling was unlikely however the high frequency of sampling meant that high frequency noise signals were detected. The raw data from measurement instruments could be plotted as a voltage signal in the time domain or transformed into the frequency domain. Figure 14 shows an example of an unfiltered time domain signal for the shaker table input acceleration on top with its frequency domain transform below. The frequency domain transform shows the band of interference along with two spikes at 12Hz and 20Hz.

4.1.2 Signal processing

In order to create a useful product from the initial voltage outputs they were scaled according to the results of calibration experiments converting them into values with suitable units to describe the response being measured. In order to ensure the reliability of the physical data output only the linear portion of the measuring instruments' responses were used in the experiment. Significant but avoidable non-linearity was found in both types of potentiometer as shown in the calibration data presented in Figure 12 below. As a result LVDT 017, for example, was set up so that the extension would only range from 10 to 30mm and a linear relationship between signal voltage and input displacement was made.

After the calibration stage the signals were then passed through a low pass filter to remove high frequency noise coming from the environment. To demonstrate the effects of filtering Figure 13 compares the amplitude of a flat noise signal before and after filtering with a low pass cut-off of 0.5Hz. There is a small transition band where frequencies are not fully attenuated nor fully transmitted around the cut-off.

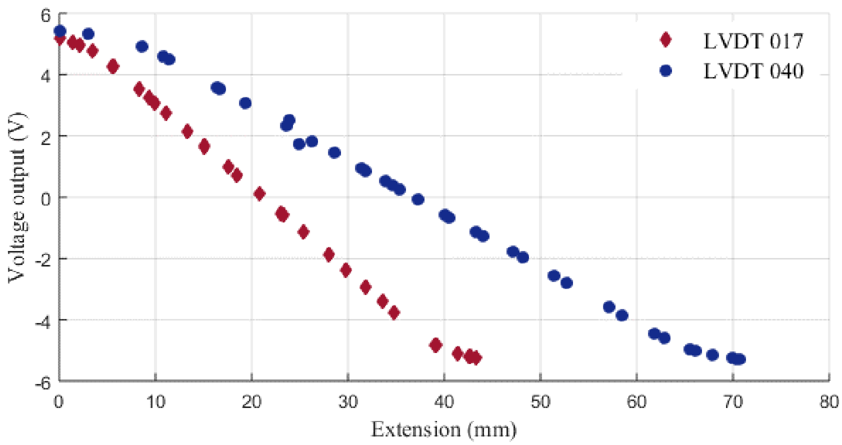

Figure 12 - LVDT calibration plot (prior to Test 1)

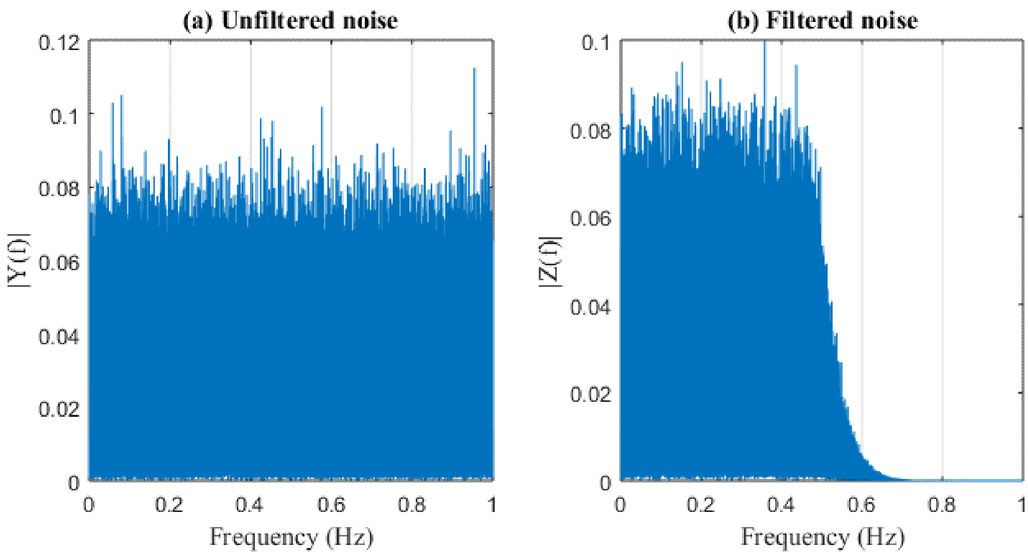

Figure 13 - Low pass filter applied to noise signal

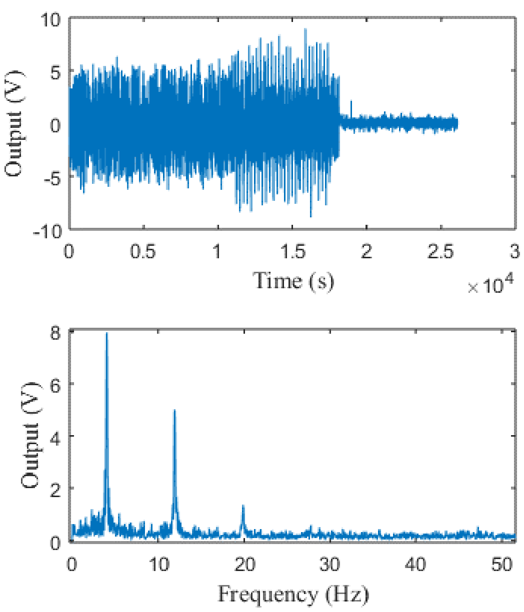

Figure 14 - Original input acceleration voltage trace

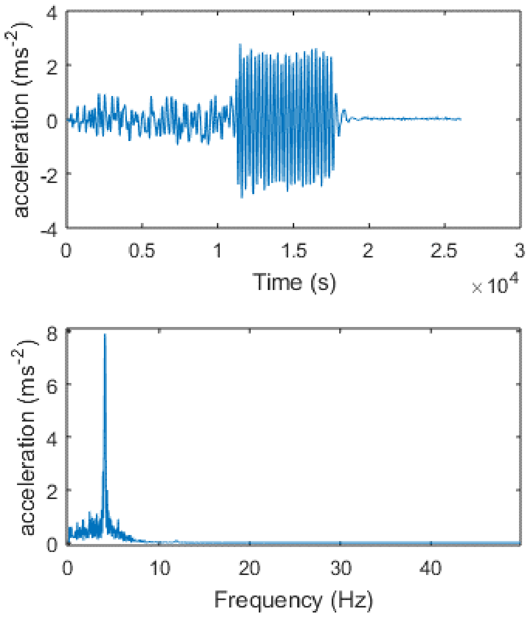

Figure 15 – Calibrated filtered input acceleration trace

4.1.3 Output signals

The product of the calibration and filtration processes can be seen in the comparison between Figure 14 and Figure 15. The time domain signal is much clearer and the reason for this can be seen in the frequency domain plots that have the high frequency interference removed.

4.2 Particle Image Velocimetry

4.2.1 Inputs – image capture

As described in section 3.1.4 the Particle Image Velocimetry analysis requires a number of specific pieces of equipment and conditions in order to be implemented successfully. The MotionBlitz camera was set out level on a tripod (see Figure 7) with flood lamps lighting up the sand reference surface. The camera was set to take images at a frequency of 100 frames per second (FPS), twenty-five times the frequency of shaking to ensure that sub-cyclic response could be tracked. The high imaging frequency meant that the shutter time (duration of opening of the camera shutter during capture of each frame) was limited to below 10ms. With the added intense illumination of the reference surface it was determined by observation of test images that a shutter time of only 1ms was required for adequate intensity. In addition to the images that were taken during the duration of each test a calibration image was taken with a Mylar card with dots at 6mm centres in place of the soil reference surface. Figure 16 and Figure 17 show respectively the calibration image and a sample image of the reference plane immediately before shaking in Test 1.1. These along with the remaining images of the reference plane during shaking form the input data for PIV analysis.

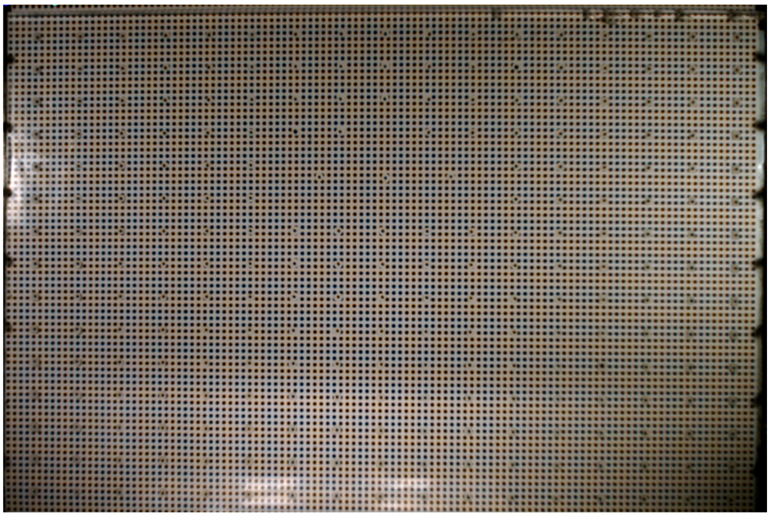

Figure 16 - PIV calibration image

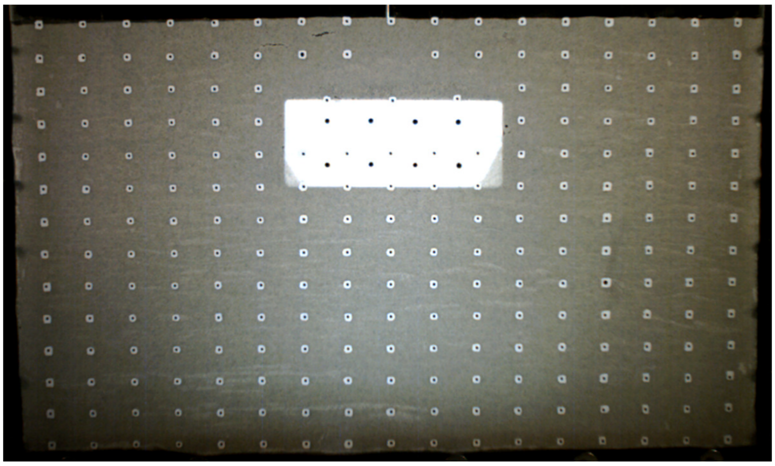

Figure 17 – Image of the soil reference plane immediately before shaking in Test 1.1

4.2.2 Process

Once the calibration and test images have been take the next step is to process them in order to generate useful results. A general process overview of PIV analysis as carried out by the available software was set out in section 2.3 and here the process is broken down into key stages for completeness as follows:

i. An area of interest was chosen from the reference plane of the soil in image space (UV coordinates).
ii. A mesh of patches was created within the area of interest at a chosen pixel size and spacing. 20 was used for each.
iii. These patches were then tracked using the geoPIV code in the image space.

For this experiment it was not possible to use the first image in each sequence as the reference due to high strains in the dynamic test meaning that patches deformed to be unrecognisable by the software and were then lost bringing a stop to the tracking. Instead a leapfrog of one was selected such that the patches in each image were tracked in comparison to the previous image reducing the number of lost patches significantly. Using the sequence of deformation movements between each frame the overall displacement of soil between any two frames could be determined.

iv. The next step was to remove the relative bulk motion between the shaking table and the camera at the same time as calibrating from UV image space to model space (XY coordinates).
v. The control markers on the inner surface of the transparent wall were located in the calibration photos and the experimental images in the UV space. Using the known spacing (6mm) of the dots on the Mylar sheet the UV coordinates of the control markers were converted into XY coordinates, fixed relative to the shaking table.
vi. The deformations expressed in the image space was then calibrated to model space giving them a scale in mm as opposed to pixels removing any optical lens deformation and removing the component of movement due to bulk translation of the shaking table throughout the cycle.

4.2.3 Outputs – quiver plots

Once the data had been processed as described in the previous section it was possible to display the deformations visually by comparing the relative deformation between any two frames of the sequence. Effectively the software takes the vector difference between the total translations of any point on the reference surface of selected frames.

The results are displayed in quiver plots that consist of an array of arrows that are rooted at the centre of each test patch that has length equal to the deformation movement in the direction of that movement. The quiver plots aid the visualisation of the soil's failure mechanism as the tunnel floats.

5 Dynamic Response of Tunnel

5.1 Horizontal Accelerations

An effect that was predicted by the finite element model of Madabhushi (2014) was the isolation of the tunnel's motion from the base movement as a result of a non-rigid connection between the base and tunnel. This isolation can be used as an indicator of the onset of liquefaction of the soil surrounding the tunnel. Figure 18 shows the accelerations from each test as labelled for the base input and the tunnel.

The comparisons show a reduction in the acceleration of the tunnel relative to the base in each of the tests except for Test 2, the test with the greatest burial ratio. In this test the peak tunnel acceleration reached between 0.9 and 1.0 times that of the input. This lack of inertial isolation observed in Test 2 suggests that the sand had not liquefied at the depth of the tunnel. As a result the tunnel was almost rigidly connected to the base via the sand at depth. This indicates a lack of liquefaction and explains the minimal floatation uplift of the tunnel itself. In this case the downward restraining forces calculated in section 3.4 were accompanied by the shear resistance of the soil. In effect the mobilisation of shear strength of the sand caused the upward buoyant force to be balanced out by the sum of the downward forces.

In contrast the three other tests saw obvious upward motion of the tunnel as a result of floatation in liquefaction. As a result it was expected that there would be a marked isolation of the tunnel motion from the base input motion and we can see this is the case for each of Tests 1, 3 and 4. In these tests where liquefaction occurred the tunnel acceleration peak value reduced to 0.54, 0.39 and 0.55 times the input peak acceleration respectively showing considerable isolation of the tunnel's movement in each case.

The three examples have some striking dissimilarities in the way in which the reduced tunnel acceleration was reached. In Test 1 the peak tunnel acceleration starts off by increasing towards the peak input acceleration and soon drops down to a steady level of isolation for the duration of shaking. Test 3 saw an initially large tunnel acceleration comparable to that of the base input which fell gradually to the final reduced level over the 26 cycles of oscillation. Test 4 had a nearly constant tunnel acceleration throughout shaking.

It is also noted that the phase difference between tunnel and input acceleration varies between each of the tests. In Test 4 the phases match almost exactly but in test three, the shallowest, the tunnel and input accelerations are in antiphase throughout.

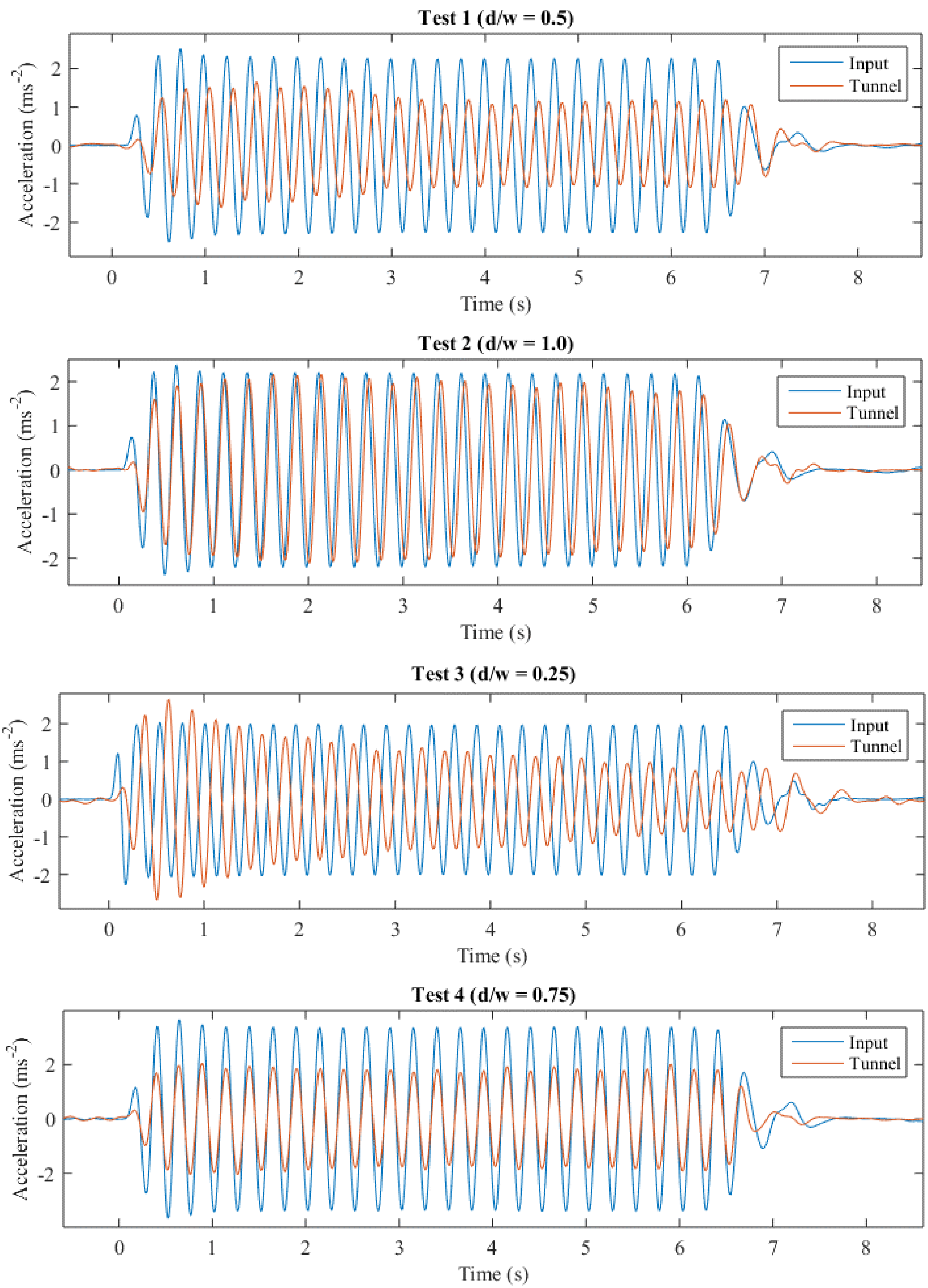

Figure 18 - Horizontal acceleration response of tunnel in comparison to base input

5.2 Vertical Displacement

Just as the isolation of horizontal accelerations of the tunnel during shaking was a result of liquefaction of the saturated Hostun sand during the shaking so is the vertical uplift of the tunnel observed in the experiment. When liquefaction occurs in the soil the shear capacity of the soil is degraded which means its contribution to restraining the buoyant uplift is reduced. When the effects of shear capacity are completely removed by full liquefaction then the floatation factors calculated in section 3.4 can apply. Even if full liquefaction does not occur the floatation factors can be used as a measure of their relative likelihood of floatation.

The tunnel uplift voltage data acquired in the tests from the draw wire potentiometer readings was scaled in accordance to the calibration data for the DWP. Figure 19 shows this data for each of the tests with positive displacement representing a vertical upwards movement of the tunnel and time zero corresponding to the time at which input oscillations were initiated. The data shown for Test 1 at R_b = 0.5 is not directly from testing but, taking the final vertical tunnel displacement and scaling the uplift data from Test 3 to represent the final displacement a trace for Test 1 can be shown.

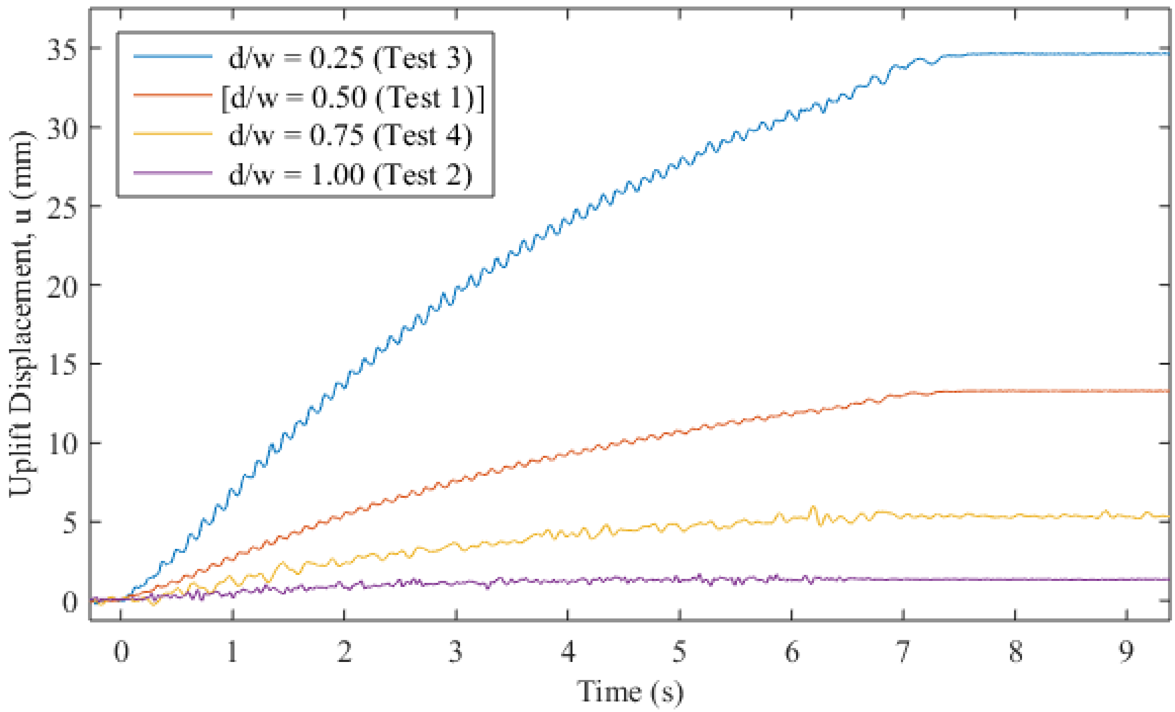

Figure 19 - Tunnel vertical displacement during shaking

In each of the cases the uplift starts almost instantly after shaking begins suggesting that the positive excess pore pressures causing liquefaction are generated quickly. At the beginning of each test the rate of uplift starts at a maximum and it steadily reduces throughout the shaking. This reduction in rate of uplift could be explained by the finite element model of Madabhushi (2014) in that the upwards motion generates negative excess pore pressures beneath the tunnel invert [7] producing a superposed downward suction force on the tunnel that begins to balance out the effect of buoyant forces. This effect of lowering the excess pore pressures beneath the tunnel invert is also observed in Room's experiments [8]. If the eventual introduction of negative excess pore pressures is able to slow down the rate of uplift it may be possible that artificially introducing negative excess pore pressures in anticipation of liquefaction could significantly reduce the damaging effects of tunnel uplift.

The maximum input oscillations stop at 6.5s (see horizontal acceleration plots of Figure 18) in each case and the uplift ceases shortly afterwards, 7s after initiation of the shaking. This slight delay between oscillations stopping and the subsequent cease to tunnel uplift suggests that the soil remains liquefied for a short time as the excess pore pressures dissipate after shaking stops.

5.2.1 Effect of burial ratio on overall tunnel uplift

The uplift data shows a clear relationship between overall tunnel uplift and burial ratio. The general relationship is one where a greater uplift is achieved for a smaller burial ratio as shown in Figure 20 where uplift is non-dimensionalised by dividing by the tunnel width. This suggests that a greater uplift corresponds to a greater extent of liquefaction as a result of fuller liquefaction occurring at smaller depth as found in section 5.1.

This inverse relationship is applicable to burial ratios greater than R_b=0.2 that would yield a maximum final uplift. At this burial ratio the crown of the tunnel is incident with the soil surface. For smaller burial ratios there would be no overburden force from soil and the buoyant force would reduce as the tunnel emerges from the tunnel surface. A neutral point at which the tunnel buoyancy balances its weight would exist, this is the limiting uplift position and would cause the plot in Figure 20 to turn and fall to zero uplift for smaller burial ratios. This information could be relevant for predicting uplift of tunnels that are subject to successive earthquakes after having come to the surface as a result of floatation previously.

5.2.2 Cyclic nature of uplift

The uplift vs time plot of Figure 19 reveals another characteristic of the uplift motion. It shows that the uplift itself has a cyclic nature. By comparing the uplift and input acceleration plots of Figure 21 it can be seen that the uplift has a cyclic behaviour at double the frequency of the input oscillations. From the relative phase of the two plots uplift is seen to occur during the quarter-cycle period centred on the input acceleration passing through zero.

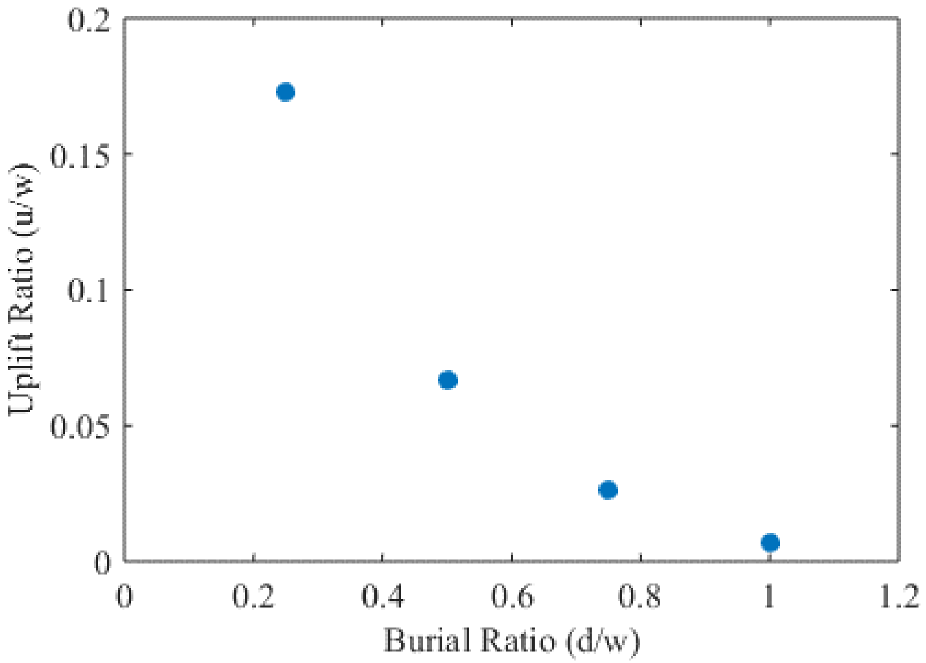

Figure 20 – Non-dimensional tunnel uplift related to burial ratio

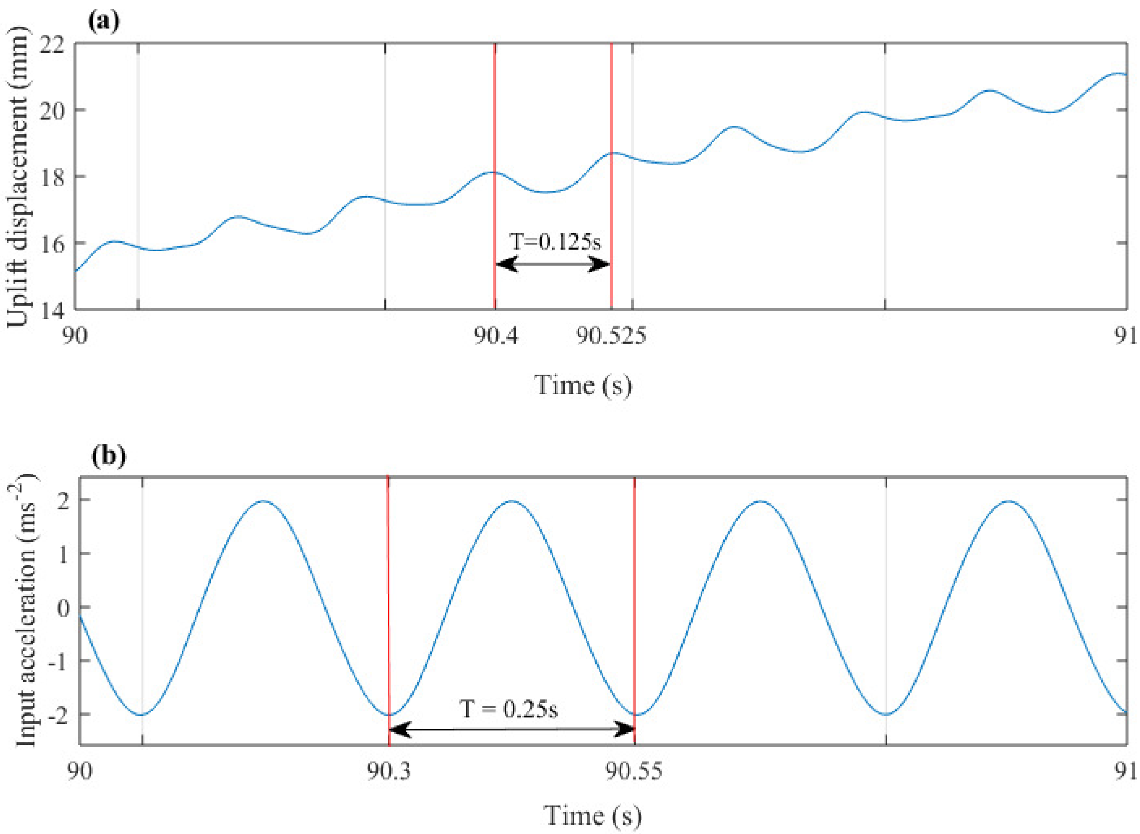

Figure 21 - cyclic phase comparison: (a) uplift displacement, (b) input acceleration

6 Soil Surface Heave and Settlement

A significant effect resulting from floatation of underground structures is heave and settlement at the soil surface. In particular surface settlement can have a detrimental effect on surface structures with shallow foundations. When soil at the depth of the foundations undergoes differential settlements the imposed tensile strains produce tensile stresses in the structure. When subjected to tensile stresses different buildings respond in different ways. Steel structures tend to fair well due to the high tensile strength of the members however masonry and concrete structures often suffer the consequences. The most common risk is when cracking exceeds the extents allowable for serviceability of the building, structural stability can also be compromised in extreme cases.

Figure 22 below shows how the soil surface profile is affected by floatation of structures at varying depths. On the left hand side are images of the reference plane in three of the earthquake tests prior to the start of shaking. The right hand side shows images of the tunnels and surrounding sand after floatation has occurred and shaking has ceased. The burial ratio, R_b, is specified for each of the pairs of images.

From the figure it is clear that the burial ratio has an influence on the resulting form of the soil surface and also the extent of the surface displacements. Where the tunnel is buried very shallow as in (a) the tunnel is able to break through the surface of the soil and comes to rest with approximately half its height above the top of the sand. It can be seen from the images that there is a near uniform 2cm downward settlement of the surface of the sand relative to the grid of white control markers that remain at a constant height throughout the tests. There is some non-uniformity around a quarter of a tunnel’s width (50mm) either side of the tunnel where there is a slight depression in the sand with the trough approximately 2mm lower than the flat sections surrounding. It is hypothesised that friction between the sand and tunnel sides had enabled the tunnel to restrain the downward soil movement close by stopping the depression in the sand coming further to the centre. As a result of the near uniform settlement either side of the tunnel the damage to nearby buildings that are not situated directly above the tunnel is likely to be limited. Buildings that are situated directly above a very shallow tunnel are likely to suffer considerable harm.

For the other two tests where the tunnel is buried deeper at burial ratios of 0.50 and 0.75 the surface profile is rather different as the tunnel sections are unable to rise above the surface. In each case the surface has a bell-shaped profile with a heightened region directly above the tunnel falling away to either side and eventually flattening out level. Where R_b =

0.50 the central section undergoes some overall heave, raising by 3mm. The sides settle by slightly more, 5mm. In contrast for the greater burial ratio of 0.75 the surface settles all over but by only 2mm directly above the tunnel and by 4mm to the sides. Structures that are situated in the vicinity are therefore susceptible to damage.

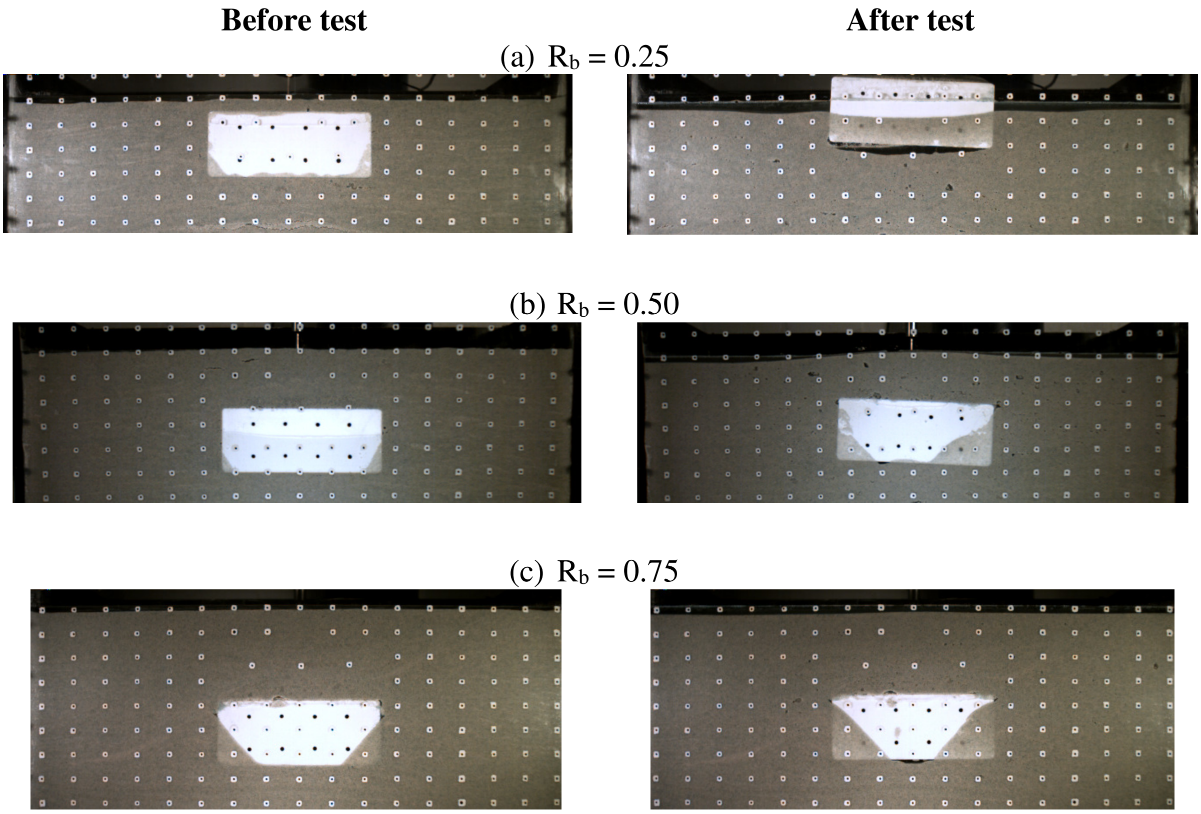

Figure 22 - surface heave and settlement for selected tests

7 Soil Deformation Mechanism

Understanding the mechanism of failure of the liquefied soil as the tunnel undergoes floatation uplift could help the development of methods of stopping the failure mechanism from being mobilised and therefore reducing floatation and its associated damages. Previous experimental work from Room and Chian (as reviewed previously) provide insight into the expected mechanism shapes exhibited by the model. Here the failure mechanism will be considered for the cumulative deformations of the soil throughout an entire earthquake. In addition the latter part considers how the failure mechanism evolves through the stages of each cycle of input movement.

7.1 Cumulative Soil Deformations

In order to allow for the tunnel movements described in previous sections it is necessary for the soil surrounding the tunnel to accommodate the motion. The liquefied soil is incompressible as it is in the undrained state and so in order to conserve mass, volume must also be conserved meaning that the soil is expected to move and deform in a particular mechanism.

Figure 5 shows the cumulative displacements of soil in the failure mechanism visualised by PIV analysis of the centrifuge modelling of a circular tunnel carried out by Chian and Madabhushi (2010). Similar results are expected for the floatation of rectangular tunnels as suggested by the observations made in rectangular tunnel testing by Room (2014).

7.1.1 Rectangular tunnels

Figure 23 and Figure 24 were produced using PIV analysis on the images captured during the earthquake tests on rectangular tunnels. Similar to the plot made for the circular tunnel these figures enable visualisation of the soil deformation with a vector field of soil displacements tracked between frames of images from the tests.

Significant differences are observed in the visualisation plots for shallow burial (R_b = 0.25) and deeper burial (R_b = 0.75). It appears that the cumulative deformation mechanism for the shallow depth tunnel is similar to those expected from Chian's testing with movement of soil downwards at the tunnel's sides and inwards and upwards beneath. One major difference is that there is very little soil above the tunnel especially once it has come to the surface. It was also observed that instead of soil filling the space left behind by the tunnel some of that space was filled by water alone in a large void beneath the whole width of the tunnel (see Figure 22 (a)).

For the deeply buried rectangular tunnel on the other hand the failure mechanism is much less pronounced. Downward movement of soil along the sides of the tunnel are visible similar to the prediction and there is also movement away from the centreline of the tunnel at the soil surface however upward movement of soil directly above and beneath the tunnel is not visible.

7.1.2 Area of influence

The area of influence of the tunnel on the surrounding soil as it floats is comparable in width to three times that of the tunnel (one tunnel's width either side). Above the tunnel the soil is generally affected all the way to the soil surface and beneath the invert of the tunnel the soil failure mechanism stretches down to a distance comparable to the tunnel height.

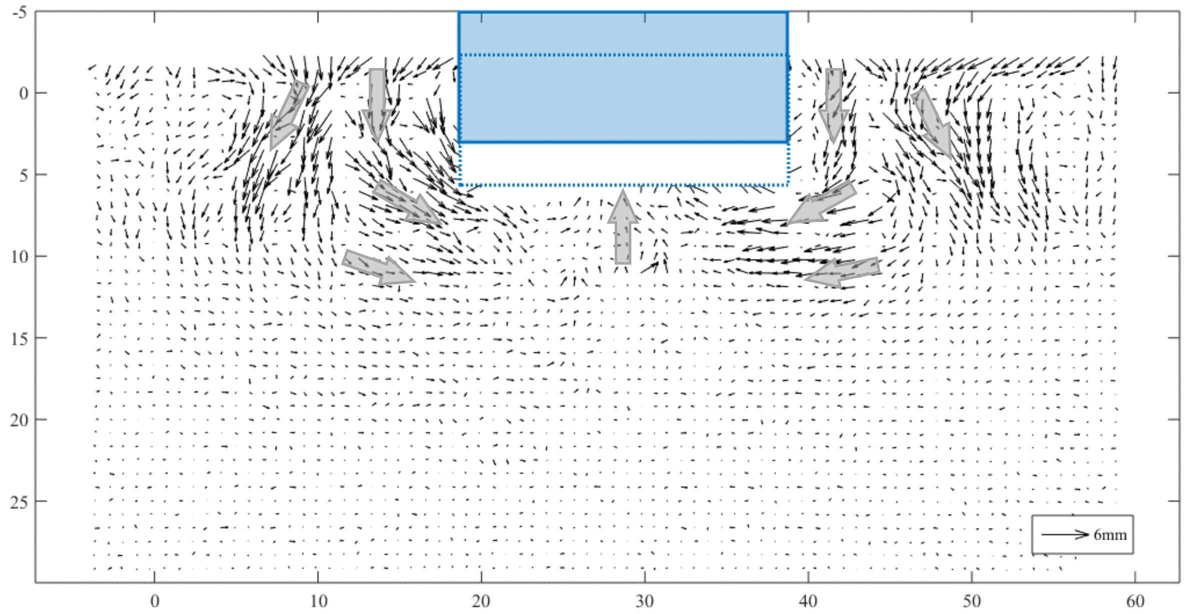

Figure 23 - Cumulative soil displacements for $R_b = 0.25$ (Test 3)

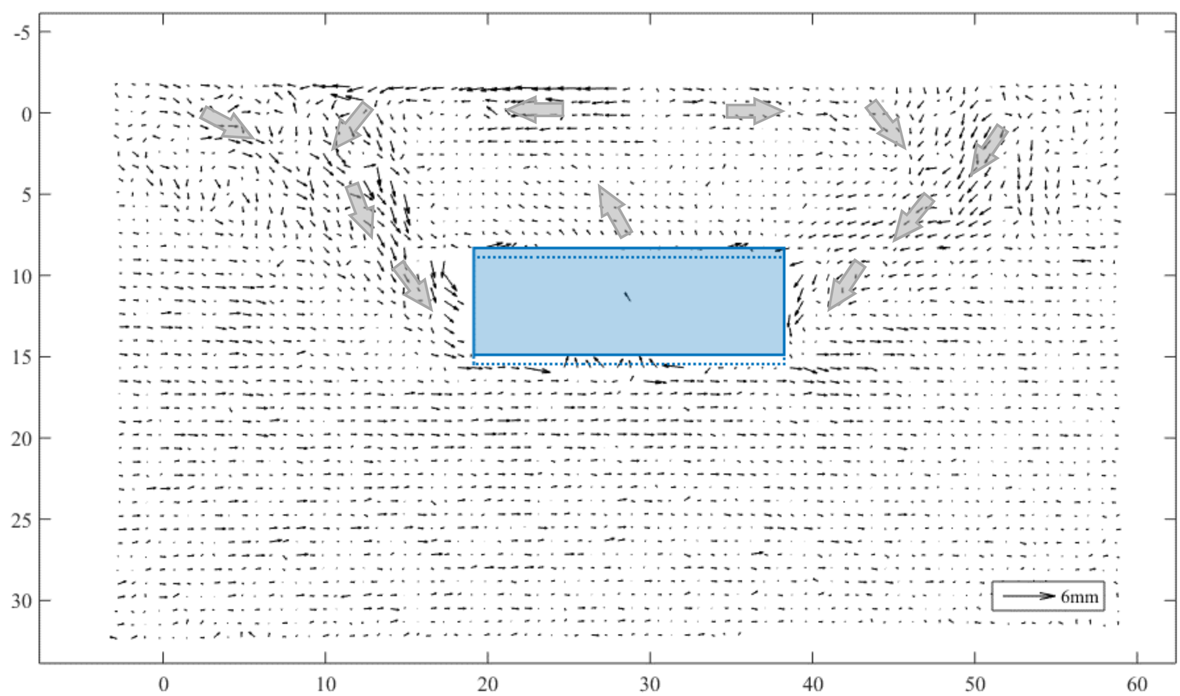

Figure 24 - Cumulative soil displacements for $R_b = 0.75$ (Test 4)

7.2 Evolution of Soil Failure Mechanism

It was shown previously that the uplift of the tunnel occurred cyclically at double the frequency of the input displacement of the shaking table. From Figure 21 it can be seen that the periods of uplift coincide with the quarter of the input cycle that starts just before zero input acceleration is reached and lasts until just before maximum input acceleration. Conversely the periods of little vertical movement and some downward settlement occur just after peak base acceleration has been reached as it falls back to zero at the zero displacement position.

In order to visualise how the soil and structure interact through each stage of this cycle their displacements were tracked to see their progression through each quarter of the input cycle. Figure 25 presents the results of this tracking with first, second, third and fourth quarter-cycle displacements being shown in (a), (b), (c) and (d) respectively.

An initial comparison between the images shows that the first and third quarter-cycle plot mechanisms are roughly a mirror image of one another, as is the case in the second and fourth quarter-cycle plots. This is expected because during the main part of shaking the input accelerations are sinusoidal in shape and therefore symmetrical.

Plots (a) and (c) of the figure correspond to the periods when maximum uplift was recorded by direct physical measurement. This uplift is confirmed by the displacement vector plots where the arrows within the bounds of the tunnel outline have a significant vertical component. Despite this the tunnel displacements are still much smaller than those of the surrounding soil. During these periods there is a large relative horizontal motion between the sand and tunnel with the tunnel having almost zero net horizontal motion throughout this phase. As the tunnel moves upwards it is clear that the soil above the tunnel is pushed upwards to make way combining with the horizontal sand motion to give it a diagonal resulting motion.

Plots (b) and (d) show the failure mechanism in the other two phases of motion where there is minimal tunnel uplift and the dominant direction of motion of the tunnel is horizontal in the direction of the surrounding soil.

Throughout the whole cycle it can be seen that the presence of the tunnel has the effect of forcing the soil to take a path of motion that goes around the obstruction. As the relative motion brings the soil towards the tunnel (e.g. on the left hand side of Figure 25 (a)) the soil is forced downwards. As the liquefied soil is incompressible and volume is conserved the soil is pushed upwards on the other side when moving away from the tunnel.

(a)
(b)
(c)
(d)

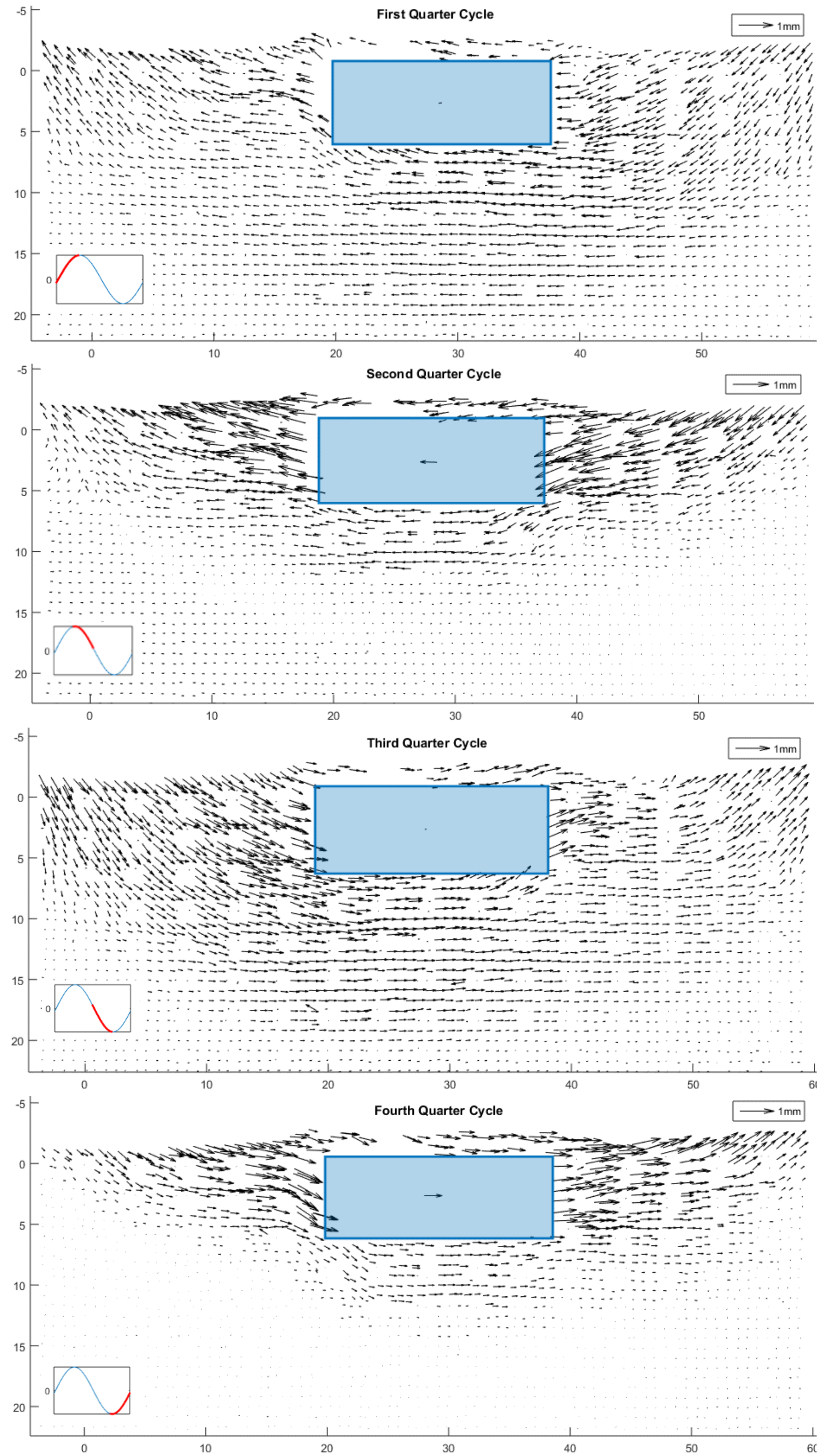

Figure 25 – Displacement vector plots for four successive quarter-cycle periods for R_b=0.25

7.2.1 Area of influence

As discussed previously the area of influence of the tunnel on the soil's deformation changes throughout the shaking cycle. In the first and third quarter-cycles when the tunnel is experiencing uplift, soil deformation is seen at a depth comparable to three times the height of the tunnel below the invert. The deformation has a large horizontal component superposed with an upward component that is a result of the negative excess pore pressures resulting from uplift beneath the tunnel invert as predicted by Madabhushi (2014). The affected depth is reduced to a third of this when there is no tunnel uplift.

7.2.2 Deformation mechanism during peak uplift

The previous section was concerned with the visualisation of soil deformation during quarter-cycle phases of the soil-structure motion with net upward and net downward motion. This section considers the mechanism of soil deformation and tunnel movement at the precise moment of peak uplift motion as these are the circumstances under which the majority of floatation occurs causing the most associated damage. Figure 26 presents the PIV deformation vector plot for this phase of motion overlaid with arrows that describe the general movement.

Here during the moment of peak uplift during the cycle it is noted that the tunnel is moving at a roughly 40° angle with the general direction of the soil's flow running perpendicular to this. The soil movements are also noted to be twice as large as the tunnel's movement which is 0.1mm in the 20ms period of deformation that this plot represents. The average velocity of the tunnel in this case is approximately 5mms^{-1}.

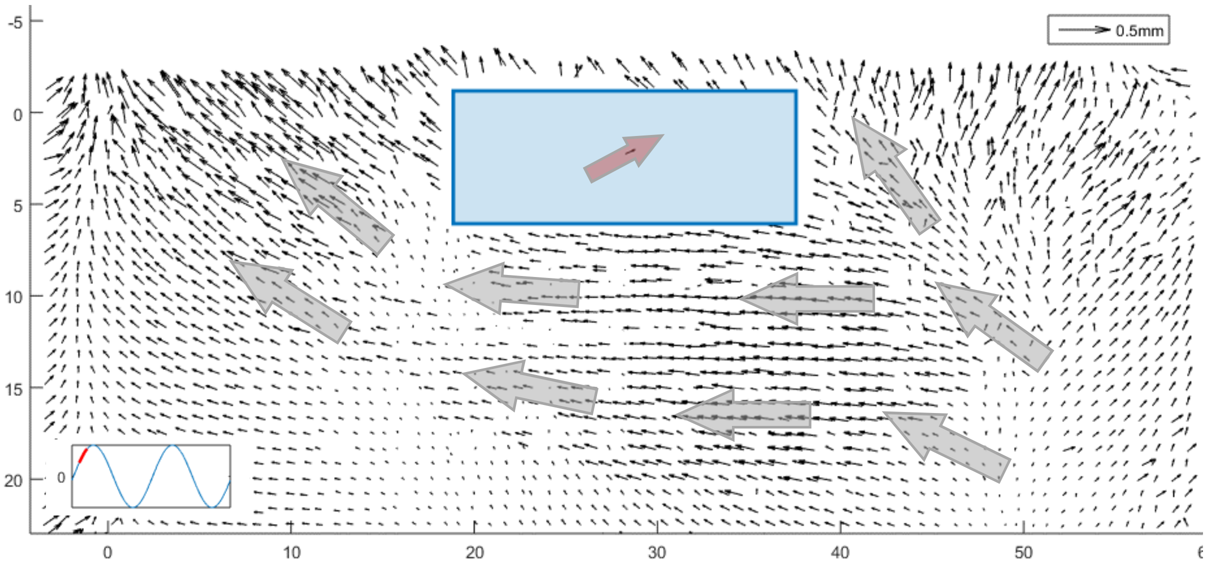

Figure 26 - Deformation vector plot for phase of peak rate of tunnel uplift

8 Conclusions

Many observations were made from the data that was acquired throughout these tests which was then interpreted to make suitable deductions. Below is a summary of the key conclusions resulting from this study.

Firstly it was found that in order for significant tunnel floatation to occur soil shear strength must be reduced, in this case by liquefaction. The extent of this liquefaction was found to be represented by comparing the peak accelerations of the structure and input oscillations giving an indicator of the isolation of motion between the tunnel and base.

When buried at deeper burial ratios tunnels experience less inertial isolation from oscillation inputs and undergo less cumulative uplift during earthquake loading. Also the mechanism of soil failure which has been shown to feature soil being pushed up around the structure and sucked up behind the tunnel's motion is much less pronounced in comparison to when the tunnel has a lower burial ratio.

The rate of overall uplift of a tunnel declines gradually throughout an earthquake input as a result of the development of negative excess pore pressures underneath the tunnel invert. Uplift continues for a short time after oscillations cease while excess pore pressure dissipate and the soil un-liquefies. If negative excess pore pressures could be introduced artificially prior to uplift occurring the effects of floatation could be significantly reduced.

Tunnel floatation uplift has a cyclic characteristic that is superimposed onto the overall uplift shape. Analysis of the cyclic uplift component shows that it occurs at double the frequency of the input oscillations and occurs during the quarter cycle that passes through zero input acceleration peaking just before maximum input acceleration is reached for any one cycle. At the moment of peak uplift the tunnel and soil are moving in diagonal perpendicular directions with the soil moving with greater speedy than the tunnel.

In floatation a tunnel influences the soil's movement up to a depth of three times the tunnel height below its invert and by approximately one tunnel's width either side.

Regardless of tunnel burial depth the surface of liquefiable soil is likely to experience an average downward settlement throughout an oscillating input due to the loosely packed structure. Generally the tunnel floatation produces a bell-shaped soil surface profile above that is accentuated as the tunnel's initial burial depth reduces. This occurs to depths until the tunnel is able to surface in which case the soil surface displacement is a near uniform downward settlement with the tunnel having punched through.

9 Scope for Future Work

Adaptations to this experiment

In order to improve the results of this experiment a number of adaptations are proposed. One significant improvement would be from increasing the resolution of the camera used to take PIV images while maintaining the high frame rate that is available.

In addition measurement of pore pressures is suggested.

Further experimentation and research

In continuation of this investigation there are a number of further areas that could be considered in future research, some possibilities include the following:

- The effect of viscosity of pore fluid on the rate of floatation. Various compounds that are dissolved or mixed into water in the environment could alter the viscosity of pore fluid. A greater viscosity would lead to increased resistance to fluid flow causing a reduced rate of pore pressure dissipation and increased resistance to rigid body motion through it.
- Similar tests could be performed in a centrifuge in order to scale the stresses to a level comparable to those expected from a full size tunnel.
- Investigate the effect on rate of tunnel uplift by artificially introducing negative excess pore pressures underneath the tunnel invert.
- Design and test floatation remediation techniques.
- Visualise the soil failure mechanism in successive earthquake motions to simulate the effects of aftershock earthquakes.

References

[1] W. H. Organisation. [Online]. Available: http://bit.ly/Jem9XC. [Accessed 1 January 2015].

[2] L. Sundermann, O. Schelske and P. Hausmann, "Mind the risk: A global ranking of cities at risk from natural disasters," Swiss Re, Zurich, Switzerland, 2013.

[3] W. Kelly, "Japan: The Anthropology of Alternate Modernity," Department of Anthropology, Yale University, 2003. [Online]. Available: http://bit.ly/1AwOm5c. [Accessed Jan 2015].

[4] Tubbi, "Broken asphalt road by Chuetsu Earthquake, 2004.," Wikimedia Commons, Ojiya, Niigata, Japan., 2004.

[5] Y. Shimbun, "Manholes sit pushed up from the ground from the recent earthquake," March 2011. [Online]. Available: http://bit.ly/1KlZ4LV. [Accessed January 2015].

[6] "Water contamination in the Christchurch area after the 22 February and 13 June 2011 earthquakes," Environment Canterbury, 7 December 2013. [Online]. Available: http://bit.ly/1dvXD3q. [Accessed 14 January 2015].

[7] S. Madabhushi and S. Madabhushi, "Finite Element Analysis of Floatation of Rectangular Tunnel Following Earthquake Induced Liquefaction," *Indian Geotechnical Journal,* 2014.

[8] E. Room, "Visualisation of floatation of tunnels following earthquake induced liquefaction," CUED, 2014.

[9] S. Chian, "Foatation of Underground Structures in Liquefiable Soils (PhD Thesis)," 2012.

[10] S. Chian and S. Madabhushi, "Use of PIV analysis for soil deformation around a tunnel in liquefiable soils," 2010.

[11] D. White, W. Take and M. Bolton, "Soil deformation measurement using particle image velocimetry (PIV) and photogrammetry," *Géotechnique,* vol. 53, no. 7, pp. 619-631, 2003.

[12] D. White and W. Take, "Particle Image Velocimetry (PIV) software for use in geotechnical testing," Cambridge University Engineering Department, Cambridge, UK, 2002.

[13] H. Mitrani, "Liquefaction remediation techniques for existing buildings," Cambridge

University, PhD Dissertation, 2006.

[14] F. Santucci de Magistris, G. Lanzano, G. Forte and G. Fabbrocino, "A database for PGA threshold in liquefaction occurrence," *Soil Dynamics and Earthquake Engineering,* no. 54, pp. 17-19, 2013.

[15] M. Dutton, "Digital Image Correlation for Evaluating Structural Engineering Materials," Kingston, Ontario, Canada, 2012.

[16] S. Chian, K. Tokimatsu and S. Madabhushi, "Soil Liquefaction-Induced Uplift of Underground Structures: Physical and Numerical Modeling," *Journal of Geotechnical and Geoenvironmental Engineering,* vol. 140, no. 10, 2014.

[17] S. Chian, "Remediation against floatation of underground structures," *Ground Improvement,* no. G13, p. August, 2013.

[18] C. Heron, "Introduction to PIV Techniques in Geotechnics," Cambridge, UK, 2013.

Appendices

A: Buoyancy calculations

The following calculations are intended to provide insight into the likelihood of floatation by floatation factors (FF) for the tunnel at the various burial ratios of the tunnel as used in the shaking tests. The floatation factor is calculated as the ratio between the upward buoyant force and the total downward restraining forces acting on the submerged tunnel. This technique was also used by Room (2014) in the analysis of rectangular tunnels.

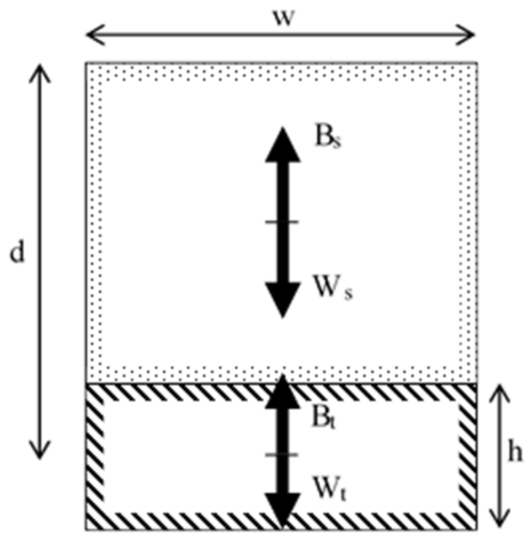

Dimension	Length (mm)
Width, w	200
Height, h	80
Length, L	300
Burial depth, d	100, 200, 50, 150

Figure 27 - Test geometry

Figure 28 - Forces acting on soil block and tunnel

Total upward Buoyancy force on tunnel,

$$F_{up} = B_t = whL\gamma_w = (0.200)(0.080)(0.300)(9.81) = 188N = 0.188kN$$

Total downward restraining forces on tunnel,

$$F_{down} = W_t + W_s - B_s = W_t + \left(d - \frac{h}{2}\right) wL[\gamma_{bulk} - \gamma_w]$$

$$= 0.0245 + \left(d - \frac{0.080}{2}\right)(0.200)(0.300)[18.64 - 9.81]$$

$= 0.0245 + (d - 0.04)(0.530)$ [kN] where d[m]

B: Test setup – sand pouring and saturation

Figure 29 - Sand pouring – sand hopper and test container

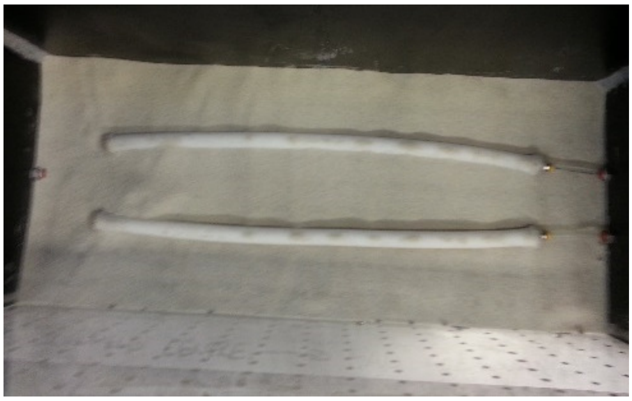

Figure 30 – Porous saturation pipes

Figure 31 – test container and saturation header tank. Sand saturation from bottom up

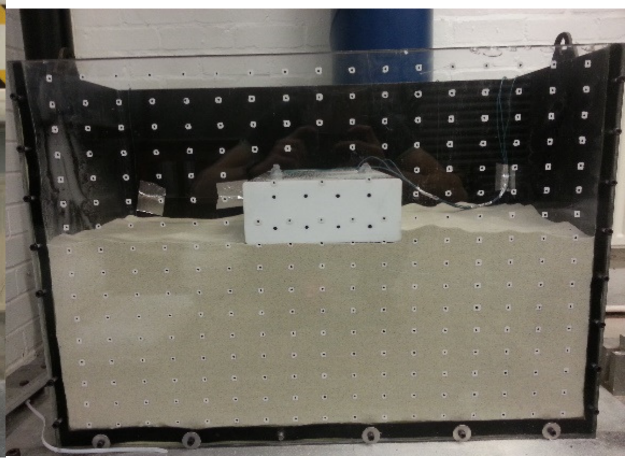

Figure 32 - Tunnel positioned during sand pouring, accelerometers fixed along rear container wall

C: Nomenclature

For reference, the symbols used in this report are summarised below:

Soil parameters	
I_D	Relative density
e	Void ratio
G_s	Specific gravity of solids
γ_{bulk}	Bulk unit weight
γ_w	Pore water unit weight

Model Tunnel Dimensions	
w; h; L	Tunnel: width; height; length
d	Depth of tunnel centroid below soil surface
R_b	Burial ratio (=d/w)
u	Tunnel uplift

Mechanical parameters	
σ; σ'	Stress: total; effective
u, u_0, Δu	Pore pressure: total; hydrostatic; excess
B_s; B_t	Buoyant force: Sand; Tunnel
W_s; W_t	Weight: Sand; Tunnel
F_{up}; F_{down}	Total force: Upward; Downward

Other	
T	Oscillatory cycle time period

Figure 33 – Summary of nomenclature

D: Risk Assessment

Before commencement of this investigation a risk assessment was conducted in order to identify possible hazards occurring from the work and to implement control measures to reduce the risk as much as practically possible to a safe level. The risks identified were predominantly related to the work that was planned to be carried out in the laboratory. Risks were related to the use of mechanical equipment such as the shaking table, electrical measuring instruments, lifting of heavy objects and inhalation of fine sand particles during model preparation. The identified main risks were all reduced effectively and no incidents were reported.

Along the course of the investigation some other risks were confronted while working in the laboratory. These included the use of a dye containing volatile solvents for colouring a fraction of the Hostun sand, it was necessary to wear respiratory equipment to prevent inhalation that would result in dizziness. The requirement for powerful lighting was identified once the project had commenced and this contributed significantly to the number of cables and leads posing a trip hazard around the apparatus. The lighting also generated considerable quantities of heat so care had to be taken when handling the equipment after use.

As a result of the fact that a number of hazards were identified after commencement of and throughout the investigation if a similar piece of work were to be attempted again formal risk assessments would be subject to review at regular intervals and updated as necessary.

One factor that could also have been considered before starting the work was hazards posed by other laboratory users. As a result of high standards of health and safety this did not turn out to be a problem at the Schofield Centre.